Resolution of Structure Characteristics of AE Signals in Multiphase Flow System—From Data to Information

Yi-Jun He, Jing-Dai Wang, Yi-Jia Cao, and Yong-Rong Yang
State Key Laboratory of Chemical Engineering, Dept. of Chemical and Biochemical Engineering,
Zhejiang University, Hangzhou 310027, P.R. China

DOI 10.1002/aic.11878
Published online July 28, 2009 in Wiley InterScience (www.interscience.wiley.com).

This investigation was performed to study the underlying structure characteristics of acoustic emission (AE) signals, which could be helpful not only to understand a relatively complete picture of hydrodynamics in multiphase flow systems, but also to extract the most useful information from the original signals with respect to a particular measurement requirement. However, due to AE signals are made up of emission from many acoustic sources at different scales, the resolution of AE signals is often very complicated and appears to be relatively poorly researched. In this study, the structure characteristics of AE signals measured both in gas–solid fluidized bed and liquid–solid stirred tank were researched in detail by resorting to wavelet transform and rescaled range analysis. A general criterion was proposed to resolve AE signals into three physical-related characteristic scales, i.e., microscale, mesoscale, and macroscale. Multiscale resolution of AE signals implied that AE signals in microscale represented totally the dynamics of solid phase and could be applied to measure particle-related properties. Furthermore, based on the structure characteristics of AE signals, useful features related to particles motion were extracted to establish two new prediction models, one for on-line measurements of particle size distribution (PSD) and average particle size in gas–solid fluidized bed and the other for on-line measurement of the suspension height in liquid–solid stirred tank. The prediction results indicated that (1) measurements of PSD and average particle size using AE method showed a fairly good agreement with that using sieve method both for laboratory scale and plant scale fluidized beds, and (2) measurements of the suspension height using AE method showed a fairly good agreement with that using visual method. The results thus validated that the extracted features based on analyses of structure characteristics of AE signals were very useful for establishing effective on-line measurement models with respect to some particular applications. © 2009 American Institute of Chemical Engineers *AIChE J,* 55: 2563–2577, 2009

Keywords: multiphase flow system, acoustic emission, structure characteristics, wavelet transform, rescaled range analysis, particle size distribution, suspension height

Introduction

Multiphase flow system exists widely in many industrial processes, such as chemical and petrochemical, metallurgy, piping transportation, pharmaceutical, and power

---

Correspondence concerning this article should be addressed to J.-D. Wang at wangjd@zju.edu.cn

© 2009 American Institute of Chemical Engineers

engineering. Despite the wide usage of multiphase systems, the thorough understanding of the hydrodynamics of multiphase systems is still a challenging problem, because multiphase flows are almost always unstable and complex spatiotemporal patterns are observed ubiquitously. Advance in computer hardware technology as well as in numerical computation methods, study of the multiphase flow patterns by computational fluid dynamics (CFD) has thus received more and more attentions in recent years.[1–7] However, establishing the exact mathematical model of multiphase systems is usually still impossible, and the experimental validation of the results of CFD simulation is also difficult; on the other hand, CFD simulation is very time-consuming, and its application to large industrial multiphase systems is not yet feasible. Therefore, various measurement techniques,[8,9] whether invasive or noninvasive, are needed both in academia and in industry, for understanding and analysis of the complex flow patterns, and for design, operation, control and scale-up purposes, respectively. Nevertheless, due to the nonlinear, nonequilibrium and multiscale characteristics of multiphase systems,[10,11] as well as each measurement technique has its own particular spatial and time resolution, none of the measurement techniques is capable of providing equally valid information over the complete spectrum of scales relevant to the complete characterization of multiphase flow systems.[9] Hence, it is recommended that several techniques may be simultaneously derived to get complementary information.[9]

Fluctuation signals collected from various measurement techniques,[9] such as pressure, ultrasound, optical fiber, and capacitance, can usually reflect a wide spectrum of complex fluctuation phenomena in multiphase flow systems. However, due to the lack of more concrete knowledge of the underlying structure characteristics of fluctuation signals, how to extract useful information from these raw fluctuation signals is still a challenging problem. Statistical characteristics (such as standard deviation, skewness, kurtosis, and entropy), obtained by simple statistical analysis of raw signals, are in general used directly for predicting the properties of multiphase systems. Because of the fact that fluctuation signals are considered commonly to be hybrid signals with multiscale components,[12–15] it could be supposed that the most useful information is only carried by some specific components at different scales with respect to a particular measurement task, such as particle size distribution, bubble size, and voidage. It is, therefore, important to separate those correlative components from original signals for extracting the most useful information. Otherwise, prediction model, established based on the above statistical characteristics of original signals, not only probably has little physical sense, but also probably has poor generalization performance.

In recent years, multi-resolution methodology has been applied to reveal the underlying multiscale characteristics of fluctuation signals.[12–15] By resorting to advanced statistical tools, such as wavelet analysis and chaos theory, some efforts have been made to explore the relationship between the decomposed components at different scales and the corresponding physical phenomena, especially for the pressure fluctuation signals in gas–solid fluidized bed system. Lu and Li[12] used wavelet analysis to pressure fluctuation signals in a bubbling fluidized bed and indicated that the level 4 detailed signal reflects the bubble behavior. Zhao and Yang[13] adopted wavelet transform to decompose pressure fluctuation signals in a fluidized bed. Hurst analysis of the decomposed fluctuation signals showed that the measured pressure fluctuations can be resolved to three characteristic scales: mesoscale signals with two distinct Hurst exponents; microscale and macroscale signals with only one characteristic Hurst exponent. Briongos et al.[14] applied the Hilbert-Huang transform method to perform a multiresolution analysis of pressure signals collected from a gas–solid fluidized bed, then the concept of averaged instantaneous frequency was used to identify three important dynamic components, such as local bubble, "bulk" and particle dynamics. Furthermore, the bulk dynamic component was used to estimate the bed expansion ratio and bed height. Yang and Leu[15] used wavelet transform to decompose the absolute pressure fluctuation signals into three scales corresponding to macroscale, mesoscale, and microscale in three circulating fluidized beds. A redefined variable, homogeneous index HI, obtained from the energy ratio of the microscale and mesoscale signals, was used to determine the transition velocities from bubbling to turbulent fluidization.

The passive acoustic emission (AE) technique has received more and more attentions in recent years as a potential nonintrusive on-line process monitoring technique to be used in multiphase flow systems.[16–22] Because of AE signals are made up of emission from many acoustic sources at different scales, the interpretation of AE signals are often very complicated. Previous studies have demonstrated that AE signals contain rich information with respect to the motion of particles.[19,22] Multiscale resolution of AE signals can thus be useful for separating the key feature information of particles motion from the original AE signals, which could help to establish physical meaningful prediction model with respect to particle-related measurement tasks. However, the underlying structure characteristics of AE signals appears to be relatively poorly investigated.[22]

The main objective of this study has been twofold: (1) to study the underlying structure characteristics of AE signals to obtain a relatively complete picture of complex hydrodynamics in multiphase flow systems; (2) to extract the most useful information from original signals with respect to a particular measurement requirement. In this study, wavelet transform and rescaled range (R/S) analysis were applied to explore and understand the structure characteristics of AE signals measured both in gas–solid fluidized bed and liquid–solid stirred tank. The structure characteristics difference between AE signals and pressure fluctuation signals in gas–solid fluidized bed was investigated. The structure characteristics of AE signals collected from gas–solid fluidized bed and liquid–solid stirred tank were compared. Furthermore, two illustrative applications of AE technique in process monitoring, i.e., particle size distribution and suspension height, were proposed to validate the effectiveness of multiscale resolution of AE signals.

Theory

Wavelet transform analysis and discrete wavelet transform

A signal may be considered as a representation with perfect time resolution. In contrast, the magnitude of the Fourier transform (FT) of the signal may be considered as a representation with perfect spectral resolution but with no time information because the magnitude of the FT conveys frequency content but it fails to convey when, in time, different events occur in the signal. FT is therefore not suited to the analysis of signals containing numerous nonstationary or transitory characteristics, such as drift, trends, abrupt changes, and beginnings and ends of events. Hence, it is important to develop effective time-frequency analysis methods so that the transform of signals may be represented in terms of both time and frequency. Two representative time-frequency analysis methods are short-time Fourier transform (STFT) and wavelet transform (WT).[23] STFT has been commonly used method for generating time-frequency representation of signals. However, STFT requires that the signal being analyzed is stationary during a short window. To improve the frequency resolution, a wider window is required. Consequently, the stationary assumption may not be valid, as well as the time resolution is decreased. On the other hand, a narrower window is required to improve the time resolution. Consequently, the frequency resolution is decreased. STFT is, therefore, less effective for analysis of transitory signals.

WT has become a very powerful time-frequency tool for analysis of nonstationary and transitory signals and has been widely applied in various fields,[24] such as signal processing, image processing, data compression and financial time series. Contrary to the Fourier-related transform methods, WT provides a more flexible way of time-frequency representation of a signal by allowing the use of variable sized windows. In WT, at high frequencies (corresponding to small scales), narrow windows are used to get precise time resolution, whereas at low frequencies (corresponding to large scales), wide windows are used to get finer frequency resolution. Localization in both frequency and time domains is thus the greatest advantage of WT over Fourier-related transform methods. Moreover, WT is often regarded as a mathematical ‘‘microscope’’ that is able to examine different parts of the signal by automatically adjusting the focus.

WT uses the wavelet function $\varphi(t)$ and scaling function $\phi(t)$ to perform simultaneously the multi-resolution analysis (MRA) decomposition and reconstruction of the measured signal. The wavelet function serving as a high-pass filter can generate the detailed version of the given signal, while the scaling function serving as a low-pass filter can generate the approximated version of the given signal. The recursive mathematical representation of MRA can be defined as follows:

$$V_{j-1} = W_j \oplus V_j = W_j \oplus W_{j+1} \oplus \cdots \oplus W_{j+L} \oplus V_{j+L} \quad (1)$$

where V_j and W_j are the approximated and detailed versions of the given signal on level j respectively; $\oplus$ denotes a orthogonal summation of two decomposed signals and L is the number of decomposition levels.

The discrete wavelet transform (DWT) can be regarded as an MRA technique, where the original signal can be decomposed into several signals with different scales or resolutions and can reconstruct the signals using inverse discrete wavelet transform. The essence of DWT is to expand a discrete signal, $x(t)$ ($t = 1,\ldots,N$), as a sum of sets of base functions $\varphi_{j,k}(t)$ and $\phi_{j,k}(t)$, which are produced by dilations and translations of the orthogonal wavelet function $\varphi(t)$ and scaling function $\phi(t)$ as follows:

$$\varphi_{j,k}(t) = 2^{-j/2}\varphi(2^{-j}t - k),\ j,k \in Z \quad (2)$$

$$\phi_{j,k}(t) = 2^{-j/2}\phi(2^{-j}t - k), \quad j,k \in Z \quad (3)$$

where j and k denote the scale and translation parameters respectively. Daubechies wavelets[25] with compactly supported properties are commonly used in wavelet analysis and have been widely applied in engineering.[13] Therefore, we use Daubechies wavelets for decomposing AE signals. Since different order of Daubechies wavelets has different compact support and can result in different decomposition errors, Daubechies wavelet with minimum decomposition error is selected in present work, i.e., Daubechies 2nd order wavelet[25] (or DAU2 for the sake of brevity).

The discrete wavelet transform of signal $x(t)$ can be obtained by

$$c_{j,k} = \langle x(t), \phi_{j,k}(t)\rangle = \int_{-\infty}^{+\infty} x(t)\overline{\phi}_{j,k}(t)dt \quad (4)$$

$$d_{j,k} = \langle x(t), \varphi_{j,k}(t)\rangle = \int_{-\infty}^{+\infty} x(t)\overline{\varphi}_{j,k}(t)dt \quad (5)$$

where $c_{j,k}$ and $d_{j,k}$ are called the approximated and detailed coefficients respectively; $\langle\cdot,\cdot\rangle$ represents inner product. Consequently, the approximated signal $A_j(t)$ and detailed signal $D_j(t)$ at each scale j can be obtained in terms of $c_{j,k}$ and $d_{j,k}$ as follows:

$$A_j(t) = \sum_k c_{j,k}\phi_{j,k}(t) \quad (6)$$

$$D_j(t) = \sum_k d_{j,k}\varphi_{j,k}(t) \quad (7)$$

Moreover, for the practical application, the approximated coefficients $c_{j,k}$ and detailed coefficients $d_{j,k}$ at scale j can be obtained in terms of the approximated coefficients $c_{j-1,k}$ at scale $j - 1$ as follows:

$$c_{j,k} = \sum_n c_{j-1,n}\langle\phi_{j,n}(t), \phi_{j-1,n}(t)\rangle = \sum_n h(n - 2k)c_{j-1,n} \quad (8)$$

$$d_{j,k} = \sum_n c_{j-1,n}\langle\varphi_{j,n}(t), \phi_{j-1,n}(t)\rangle = \sum_n g(n - 2k)c_{j-1,n} \quad (9)$$

where $h(n)$ and $g(n)$ denote the low-pass filter and high-pass filter coefficients respectively.

According to the theory of MRA shown in Eq. 1, the approximated signal $A_{j-1}(t)$ on level $j - 1$ can be decomposed into the approximated signal $A_j(t)$ and detailed signal $D_j(t)$ on level j presented as

$$A_{j-1}(t) = A_j(t) + D_j(t) \tag{10}$$

The signal $x(t)$ can thus be reconstructed in terms of these decomposed orthogonal signals on different levels:

$$x(t) = A_L(t) + D_L(t) + \cdots + D_1(t) = A_L(t) + \sum_{j=1}^{L} D_j(t) \tag{11}$$

The energy percentages of the approximated signal $A_L(t)$ and detailed signal $D_j(t)$ can be described as follows:

$$\mathrm{EP}_{L,A} = \frac{E_{L,A}}{E} = \frac{1}{E}\sum_{t=1}^{N} |A_L(t)|^2 \tag{12}$$

$$\mathrm{EP}_{j,D} = \frac{E_{j,D}}{E} = \frac{1}{E}\sum_{t=1}^{N} \left|D_j(t)\right|^2, \quad j = 1, \ldots, L \tag{13}$$

where $E_{L,A}$ and $\mathrm{EP}_{L,A}$ are the energy and energy percentage of the approximated signal $A_L(t)$ respectively; $E_{j,D}$ and $\mathrm{EP}_{j,D}$ are the energy and energy percentage of the detailed signal $D_j(t)$ respectively; E is the total energy of $x(t)$ defined by

$$E = \sum_{t=1}^{N} |x(t)|^2 = \sum_{t=1}^{N} |A_L(t)|^2 + \sum_{j=1}^{L}\sum_{t=1}^{N} \left|D_j(t)\right|^2 \tag{14}$$

The energy distribution of $x(t)$ can thus be obtained by calculating Eqs. 12–14 under various levels.

Rescaled range analysis, Hurst exponent, and fractal dimension

Rescaled range (R/S) analysis, originally developed by an Egyptian hydrologist Hurst (1951) to analyze Nile River's overflows,[26] can identify long-range dependence in highly non-Gaussian time series and detect nonperiodic cycles. Moreover, it provides an effective way for studying the fractal characteristics of a time series. Recent years, R/S analysis has been applied by a number of groups to characterize the complex hydrodynamics of multiphase flow systems.[13,22,27–30] In this study, this type of analysis is adopted to analyze the decomposed AE signals on different levels, and a criterion is further established to resolve the AE signals into three characteristic scales in terms of different fractal characteristics.

The detailed implementation of R/S analysis for estimating the Hurst exponent, H, is described as follows.[13]

Step 1: Divide the discrete time series $x(t)$ ($t = 1,\ldots,N$) into $N_s = \mathrm{int}(N/\tau)$ nonoverlapping subseries of equal length τ. Because the length N of the series is often not a multiple of the considered time scale τ, a short part at the end of the time series is discarded.

Step 2: Calculate the mean and standard deviation, M_k, and S_k

$$M_k = \frac{1}{\tau}\sum_{t=(k-1)\tau+1}^{k\tau} x(t) \tag{15}$$

$$S_k = \sqrt{\frac{1}{\tau}\sum_{t=(k-1)\tau+1}^{k\tau} (x(t) - M_k)^2} \tag{16}$$

for each subseries k, $k = 1,\ldots,N_s$.

Step 3: Calculate the range R_k

$$z_i = \sum_{t=(k-1)\tau+1}^{(k-1)\tau+i} (x(t) - M_k) \tag{17}$$

$$R_k = \max_{i\in\{1,\ldots,\tau\}}\{z_i\} - \min_{i\in\{1,\ldots,\tau\}}\{z_i\} \tag{18}$$

for each subseries k, $k = 1,\ldots,N_s$.

Step 4: Rescale the range R_k by dividing the standard deviation S_k, i.e., R_k/S_k, for each subseries k, $k = 1,\ldots,N_s$. Then, average over all rescaled statistics R_k/S_k for a specified time scale τ as follows:

$$(R/S)_\tau = \frac{1}{N_s}\sum_{k=1}^{N_s} (R_k/S_k) \tag{19}$$

For each time scale τ, it is expected that the averaged rescaled statistics $(R/S)_\tau$ displays the scaling behavior as follows[30,31]:

$$(R/S)_\tau \propto \tau^H \tag{20}$$

where H is the Hurst exponent. Hence, after the analysis is conducted for all possible time scale τ, we can plot log(R/S) against log(τ). By performing a linear least-squares regression, the slope of the regression which is the estimate of the Hurst exponent H can be obtained. If the Hurst exponent equals to 0.5, the time series is random. If the Hurst exponent is greater than 0.5, the time series is persistent. Persistent implies that if the trend of the time series has increased or decreased, then the chances are that it will continue to increase or decrease in the future, respectively. Moreover, the strength of trend-reinforcing behavior, or persistence, increases as the Hurst exponent approaches 1.0. Conversely, if the Hurst exponent is less than 0.5, the time series is antipersistence. This means that, whenever the trend of the time series has increased, it is more likely that it will decrease in the close future. The strength of antipersistent increases as the Hurst exponent approaches 0. It is important to note that persistent time series have little noise whereas antipersistent time series show presence of high-frequency noise. The relationship between the fractal dimension D_F of the time series and the Hurst exponent H can be expressed as follows:

$$D_F = 2 - H \tag{21}$$

Experimental

Gas–solid fluidized bed

The gas–solid multiphase flow experiments were carried out in gas–solid fluidized beds both for cold mode in laboratory scale and hot model in plant scale. A schematic diagram of the laboratory scale cold mode experimental apparatus

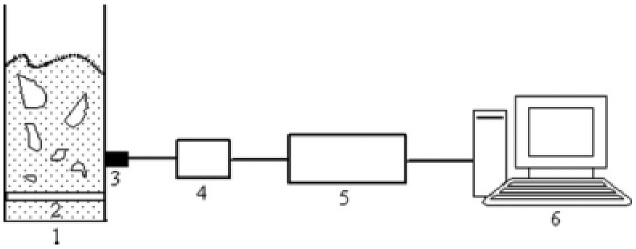

Figure 1. Schematic diagram of experimental apparatus of gas–solid fluidized bed.

1 – Fluidized bed; 2 – Distributor; 3 – AE sensor; 4 – Preamplifier; 5 – main amplifier; 6 – Computer.

used in the present study is shown in Figure 1. It consists of two parts: a fluidized bed and an AE signal collection system. The fluidized bed assembly includes a plexiglass bed (150 mm in i.d. and 1000 mm in height) and a perforated-plate distributor (with a pore diameter of 2.0 mm and a fractional open area ratio of 2.6%). Three types of polyethylene (PE) particles: linear low-density polyethylene (LLDPE), high-density polyethylene (HDPE) and bi-mode polyethylene (BPE), were used as the fluidized particles. Seven different particle sizes of these three types of PE, 0.14, 0.18, 0.36, 0.50, 0.71, 1.19, and 2 mm, were selected by sieving. The fluidized media is air at a velocity range of 0–1.1 m s^{-1}. The AE signal collection and analysis system, developed by the UNILAB Research Center of Chemical Engineering at Zhejiang Univeristy, consists of an AE sensor, a preamplifier, a main amplifier and a control computer with an A/D conversion module. The AE sensor was attached close to the wall of the fluidized bed at a location 150 mm above the gas distributor. Based on the Shannon sampling theorem, which indicates the sampling frequency must be twice the highest frequency components of the signal, a sampling frequency of 500 kHz is determined.

The plant scale hot mode experiments were conducted in three industrial fluidized beds for production of LLDPE, HDPE, and BPE. The i.d. and height of LLDPE, HDPE, and BPE industrial fluidized beds are 3500 mm and 12 m, 3500 mm and 15 m, and 5000 mm and 18 m, respectively. The AE sensors were installed at a location 1000 mm above the gas distributor for these three industrial fluidized beds, with a sampling frequency of 500 kHz. The operating gas velocities for LLDPE, HDPE and BPE industrial fluidized beds are 0.6 m s^{-1}, 0.6 m s^{-1}, and 0.4 m s^{-1}, respectively.

Liquid–solid stirred tank

The liquid–solid multiphase flow experiments were carried out in a stirred tank. Figure 2 is a schematic diagram of the experimental apparatus used in the present study. It consists of two parts: a stirred tank and an AE signal collection system. The stirred tank assembly includes a tank (with a diameter of 105 mm and a height of 150 mm) and an impeller. Two types of impeller, 6-bladed disk turbine (with a diameter of 55 mm) and 2-bladed paddle impeller (with a diameter of 65 mm), were chosen. The impeller was installed at a height of 15 mm above the bottom of the tank. The impeller speed was measured using an electronic constant agitator and is accurate to ±10 r min^{-1}. The stirred tank is charged with water with as a density of 1000 kg m^{-3} as the liquid phase, and glass beads with a density of 2250 kg m^{-3} as the solid phase. The glass beads with three different diameters (0.3, 0.5, and 0.7 mm) and two different concentrations (0.13 and 0.016 g mL^{-1}), were investigated.

The AE sensors were installed at 24 different axial heights, starting from a height of 5 mm to a height of 120 mm. The distance between any two adjacent AE sensors is 5 mm. A sampling frequency of 100 kHz is determined in terms of the Shannon sampling theory.

AE measurement and source of AE signals

The AE sensors used in this study is a kind of piezoelectric resonant accelerometer, which is broadly used in collecting the acceleration of vibration without the noise transferred via the air. The Parameters of the AE sensor used in the experiments are shown as follows: resonance frequency is 300 kHz, band width at 10 dB is 80–400 kHz and sensitivity is >65 dB. An acoustic coupling agent is used to transfer the acoustic emission in the vessel to the transducer. For temporary installations, silicone grease is used to hold the transducer in place. For permanent installations, an adhesive holds the transducer in place and acts as an effective acoustic-coupling agent. The preamplifier (PXPA III, China) supplies sufficient gain for the signal to be ‘‘driven’’ down a cable, which can be up to 200 m in length. The gain of preamplifier is 40 dB, and the RMS noise of preamplifier is 2.8 μV under the condition of input short-circuit. The main amplifier used in the experiments is PXMA signal conditioning equipment (PXMA, China). The data acquisition system consists of a data acquisition card (NI PCI-6071E, Nation Instruments) and a personal computer. The AE signals generated by the piezoelectric accelerometer are amplified, and conditioned. Finally, they are transferred to the data acquisition card connected to the computer, controlled by the software package Labview.

The AE signal detected by piezoelectric accelerometer could be considered as mechanical vibration signal. In gas–solid fluidized bed, several dynamical vibrations come from different sources, such as particle-wall impact, particle-particle collision, and macrocirculation patterns. Piezoelectric accelerometer fixed on the wall is more sensitive to the particle-wall impact, while vibrations generated from particle-particle collision and macrocirculation patterns attenuate quickly in air and not so easy to be detected by accelerometers. On the other hand, in liquid–solid stirred tank, dynamical vibrations are generated not only by the collisions between particles and tank, but also by the collisions

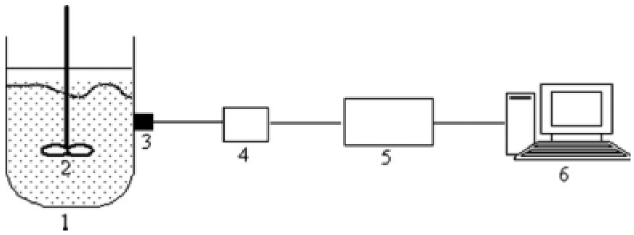

Figure 2. Schematic diagram of experimental apparatus of liquid–solid stirred tank.

1 – Stirred tank; 2 – Impeller; 3 – AE sensor; 4 – Preamplifier; 5 – main amplifier 6 – Computer.

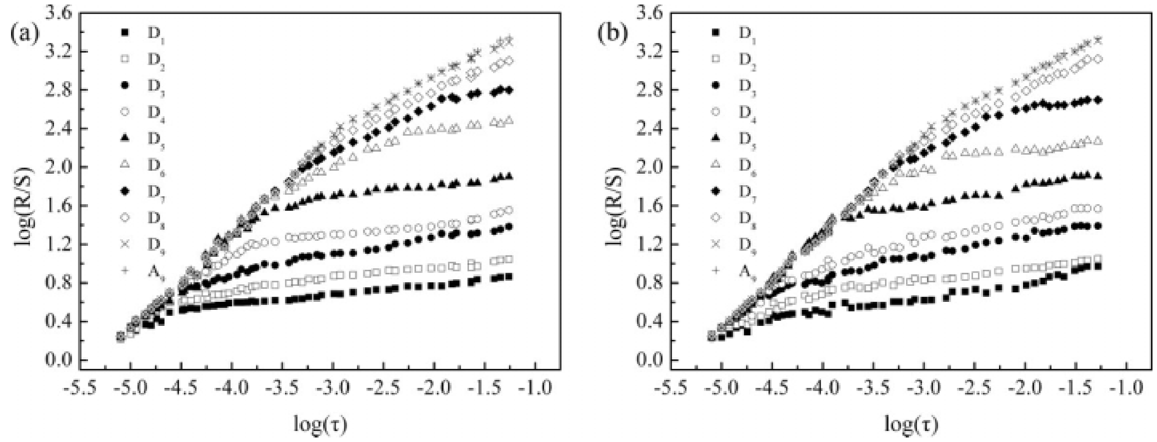

Figure 3. log(R/S) vs. log(τ) for decomposed signals for different particle sizes (a) 0.159 mm (b) 0.565 mm.

between liquids and tank. Both vibrations could be detected by piezoelectric accelerometer.

Results and Discussion

Structure characteristics comparison between AE signals and pressure fluctuation signals

One type of PE particles, i.e., BPE, with four different average particle sizes of 0.159, 0.365, 0.565, and 0.942 mm, was investigated to study the structure characteristics of AE signals. Fluidization was performed in the laboratory scale cold mode fluidized bed at a superficial gas velocity of 0.103 m s^{-1}. The original AE signals from four different measurements, corresponding to four different particle sizes, were decomposed to 1–9 level detailed signals (D_1–D_9) and level-9 approximated signal (A_9) using Daubechies 2nd order wavelet transform.[25] The R/S analysis is further applied to the detailed signals D_1–D_9, as well as the approximated signal A_9. Figure 3 shows two plots of log(R/S) against log(τ), corresponding to two different particle sizes of 0.159 mm and 0.565 mm, respectively. It is observed that the R/S curves for different particle sizes have the similar characteristics as shown in Figures 3a, b. Furthermore, it can be seen from Figures 3a, b that (1) there are two distinct linear regions of log(R/S) vs. log(τ) for the detailed signals D_1–D_5, as well as that for the detailed signals D_8–D_9 and the approximated signal A_9, indicating bifractal characteristics in those signals, (2) there are three distinct linear regions of log(R/S) vs. log(τ) for the detailed signals D_6–D_7, indicating more complex multifractal characteristics in those signals.

By performing the least-squared regression, Table 1 shows the Hurst exponents of decomposed signals for different particle sizes. It can be seen from Table 1 that two distinct Hurst exponents for the detailed signals D_1–D_5 of all different particle sizes, H_2 from the slope at smaller τ and H_3 from the slope at larger τ, are found to be much less than 0.5. Both Hurst exponents less than 0.5 indicate that the detailed signals D_1–D_5 are much irregular and represent an antipersistence behavior in gas–solid fluidized bed. Because the mechanism of acoustic emissions generated in gas–solid fluidized bed mainly owe to the collisions between particles and wall, which reflects the microscale interaction behavior among particles and between particles and fluid, the irregular and high-frequency detailed signals D_1–D_5 can be considered to imply the complex microscale motion of solid phase. Moreover, according to the wavelet analysis, the frequency band of the detailed signals D_1–D_5 lies within (15.63 kHz, 500 kHz) being consistent with the main frequency band in a normal fluidized bed,[21] which further supports the aforementioned implication.

Table 1. Hurst Exponents of Decomposed Signals for Different Particle Sizes

Particle Size (mm)		Decomposed Signal									
		D_1	D_2	D_3	D_4	D_5	D_6	D_7	D_8	D_9	A_9
0.159	H_1	–	–	–	–	–	0.984	0.989	0.998	0.992	0.995
	H_2	0.275	0.244	0.288	0.283	0.289	0.496	0.512	0.639	0.671	0.673
	H_3	0.105	0.133	0.195	0.178	0.184	0.168	0.195	–	–	–
0.365	H_1	–	–	–	–	–	0.996	0.996	0.998	0.996	0.996
	H_2	0.217	0.238	0.275	0.249	0.289	0.494	0.529	0.616	0.666	0.661
	H_3	0.095	0.126	0.18	0.108	0.13	0.168	0.177	–	–	–
0.565	H_1	–	–	–	–	–	0.995	0.995	0.995	0.996	0.995
	H_2	0.25	0.242	0.218	0.273	0.291	0.489	0.518	0.653	0.662	0.67
	H_3	0.145	0.215	0.165	0.171	0.187	0.191	0.197	–	–	–
0.942	H_1	–	–	–	–	–	0.997	0.997	0.998	0.998	0.997
	H_2	0.27	0.252	0.316	0.281	0.295	0.488	0.518	0.553	0.662	0.67
	H_3	0.135	0.211	0.168	0.183	0.189	0.167	0.205	–	–	–

Three distinct Hurst exponents, H_1, H_2, and H_3 being the slopes at smaller, medium and larger τ respectively, are shown in Table 1 for the detailed signals D_6–D_7 of all different particle sizes. It can be seen from Table 1 that (1) the Hurst exponent H_1 at smaller τ is much greater than 0.5 and almost approaches to 1.0, which indicates a highly persistent hydrodynamics feature of the gas–solid fluidized system, (2) the Hurst exponent H_2 at medium τ roughly equals to 0.5, which indicates a random hydrodynamics feature of the gas–solid fluidized system, and (3) the Hurst exponent H_3 at larger τ is much less than 0.5, which indicates a highly anti-persistent hydrodynamics feature of the gas–solid fluidized system. Generally, there are mainly two types of particles motions in gas–solid fluidized bed, particles motion along with solid phase and particles motion along with bubble phase respectively. Meanwhile, it is in general considered that the motion of bubble phase is more regular than that of solid phase. Therefore, the detailed signals D_6–D_7 imply complex mesoscale interaction between solid phase and bubble phase, where the Hurst exponent H_1 at smaller τ represents a hydrodynamic feature of bubble phase and the Hurst exponent H_3 at larger τ represents a hydrodynamic feature of solid phase. It can also be seen from Table 1 that the Hurst exponent H_2 at medium τ is a little less than 0.5 for the detailed signal D_6 and that is a little greater than 0.5 for the detailed signal D_7. This implies that the detailed signals D_6 and D_7 can be seen as the mesoscale interaction in a fluidized bed mainly dominated by the motions of solid phase and bubble phase respectively. Moreover, it can be seen from Figures 3a, b that the curves of the detailed signals D_6 and D_7 in the log(R/S) vs. log(τ) plots will begin to approach to the microscale signals (e.g., the detailed signals D_5) as the particle size increases, and vice versa. This means that the effect of the motion of solid phase on the mesoscale interaction in a fluidized bed increases as the particle size increases.

Two distinct Hurst exponents, H_1 from the slope at smaller τ and H_2 from the slope at larger τ, are shown in Table 1 for the detailed signals D_8–D_9 and the approximated signal A_9 of all different particle sizes. Both Hurst exponents are found to be much greater 0.5, which indicates that the detailed signals D_8–D_9 and the approximated signal A_9 are regular and represent a persistence behavior in the gas–solid fluidized bed. Therefore, the detailed signals D_8–D_9 and the approximated signal A_9 can be considered to represent the whole macroscale interaction of the fluidized bed.

According to the aforementioned R/S analysis of the decomposed AE signals, a relatively complete picture of hydrodynamics in gas–solid fluidized bed can be described. Similar with the study of Zhao and Yang,[13] these decomposed signals are further synthesized into three characteristic scales in terms of Hurst exponent characteristics: microscale signals with all Hurst exponents less than 0.5; mesoscale signals with some Hurst exponents less than 0.5 and some Hurst exponents greater than 0.5; macroscale signals with all Hurst exponents greater than 0.5. Microscale, mesoscale and macroscale signals represent microscale interaction behavior of solid phase, mesoscale interaction behavior between solid phase and bubble phase, and macroscale interaction behavior of fluidized bed respectively. An example of three-scale resolution of AE signals for BPE with a particle size of 0.365 mm is shown in Figure 4.

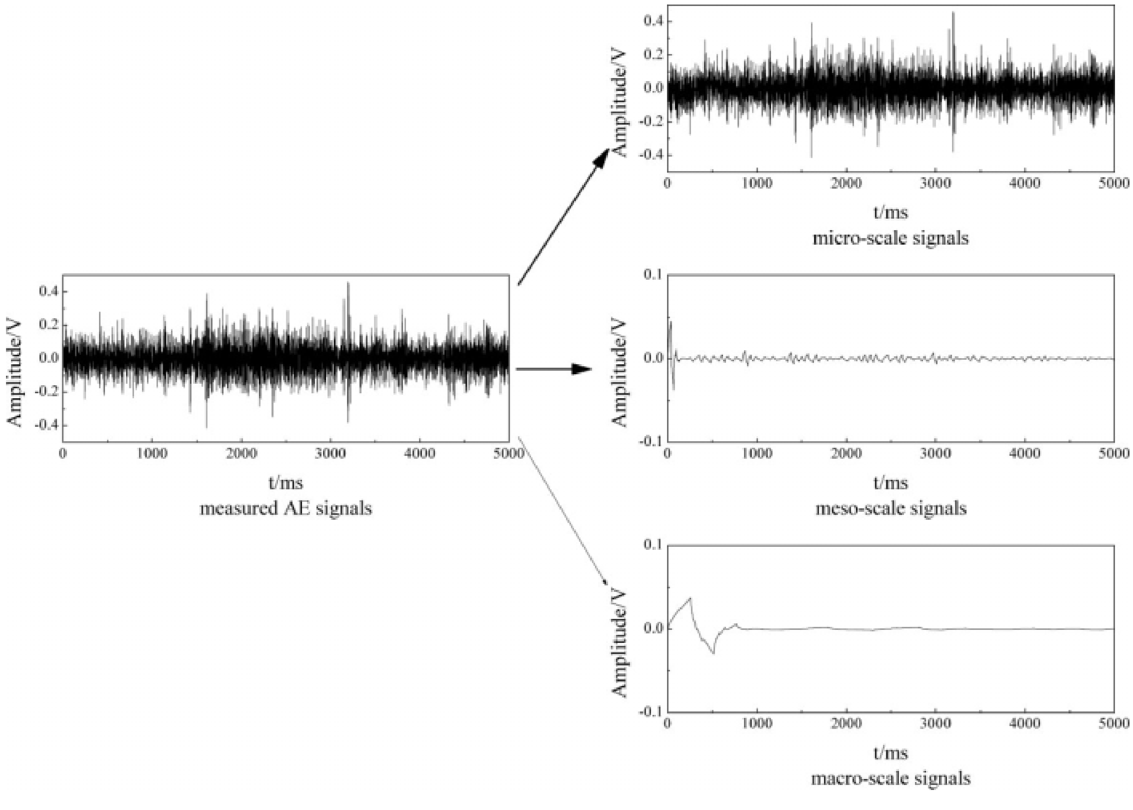

Figure 4. Resolution of measured AE signals into three scales for BPE with a particle size of 0.365 mm.

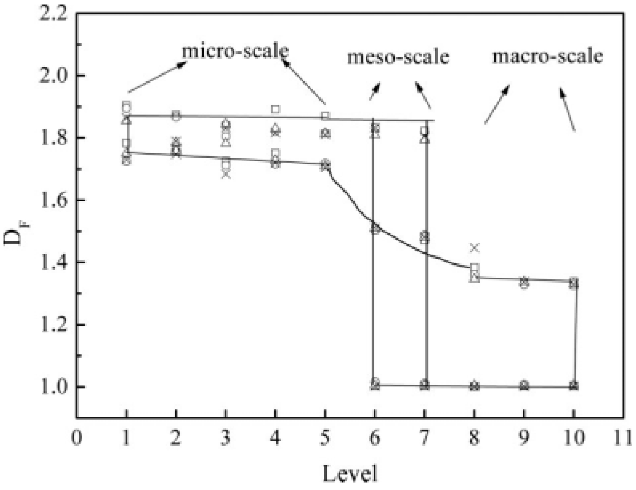

Figure 5. Structure diagram of AE signals.

Particle size: 0.159 mm(○); 0.365 mm (□); 0.565 mm (△); 0.942 mm(×).

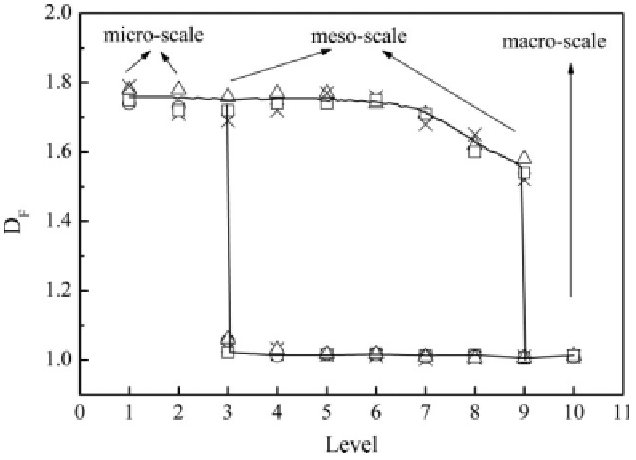

Figure 6. Structure diagram of pressure signals.

Height: 0.09m (□); 0.20 m (○); 0.40 m (×); −0.12 m (△).

To perform the structure characteristics comparison between AE signals and pressure fluctuation signals, a plot of fractal dimension D_F against level, called structure diagram in the present study, is adopted. Figures 5 and 6 show the structure diagrams of AE signals and pressure signals respectively (for ease of explanation, level 10 in both Figures 4 and 5 is actually a level 9 approximated signal), where the result of Figure 6 is derived from the previous study of Zhao and Yang.[13] It can be seen from Figure 5 that (1) microscale signals consist of 1–5 level detailed signals, (2) mesoscale signals consist of 6–7 level detailed signals, and (3) macroscale signals consist of 8–9 level detailed signals and level 10 approximated signals. It can be seen from Figure 6 that (1) microscale signals consist of 1–2 level detailed signals, (2) mesoscale signals consist of 3–9 level detailed signals, and (3) macroscale signals consist of level 10 approximated signals.

Moreover, by calculating the energy percentages for all decomposed AE signals based on Eqs. 12 and 13, the energy percentages, R_s, for microscale, mesoscale, and macroscale signals can be obtained shown in Table 2 for different particle sizes. It can be seen from Table 2 that the most energy is distributed mainly by microscale signals consisting of the level 1–5 detailed signals, and is over 95% of the total energy. It can also be seen that the energy percentage of mesoscale signals increases as the particle size increases, which may be caused by the fact that the effect of the motion of solid phase on the mesoscale interaction between solid phase and bubble phase increases as the particle size increases. Correspondingly, as Zhao and Yang stated,[13] the most energy of pressure signals is distributed mainly by mesoscale signals consisting of the level 3–9 detailed signals, and is over 90% of the total energy.

Via the analyses of the structure characteristics of AE and pressure signals, the main difference between them can be summarized that (1) AE signals in microscale contain the most information of the original signals and represent totally the dynamics of particles motion; (2) pressure signals in mesoscale contain the most information of the original signals and represent the interaction dynamics of solid phase and bubble phase.[13] Because the most information about particles motion is coupled strongly with bubbles motion in mesoscale pressure signals, it is difficult to separate that key information about particles motion from the original signals. Consequently, it hinders the applications of pressure technique to measure particle-related properties. In contrast, it is easy to separate the information about particles motion from AE signals by resorting to multiscale decomposition. Consequently, AE technique can be considered as a potential method for its application to on-line measurement of particle-related properties.

In a word, based on the aforementioned thorough investigations of underlying structure characteristic of AE and pressure signals, it is, therefore, helpful not only to choose a more suitable measurement technique with respect to measurement requirement, but also to establish physical meaningful prediction model. AE measurement technique is more suitable for measuring particle-related properties (e.g., particle size, particle size distribution, and particle density etc.), whereas pressure measurement technique is more suitable for measuring bubble-related properties (e.g., bubble size, bubble velocity, and wake vortex etc.).

Measurement of average particle size and particle size distribution

The average particle size and particle size distribution (PSD) have significant effects not only on the properties of final products, but also on the performance of gas–solid

Table 2. Energy Distribution for Multiscale AE Signals

Particle Size (mm)	0.159			0.365			0.565			0.942		
Scale	Micro	Meso	Macro	Micro	Meso	Macro	Micro	Meso	Macro	Micro	Meso	Macro
R_S (%)	98.96	1.02	0.02	97.95	2.03	0.02	97.65	2.33	0.02	97.36	2.62	0.02

fluidized beds, especially with respect to the polymerization of olefins in fluidized beds. Therefore, the developments of effective on-line monitoring techniques for both average particle size and PSD measurements are very essential. One of the most widely used methods to determine average particle size, as well as PSD, is manual sieve analysis. However, sieve analysis can not satisfy the real-time requirement because of its long sampling interval. Optical measurement technique can not be suitable for the stringent industrial environment, and its applications in industrial fluidized beds are rarely reported in open literature. Moreover, in view of the fact that the rays (e.g., χ-ray, and γ-ray etc.) are harmful to human health, it hinders their applications as measurement techniques. Therefore, the invention of a novel on-line measurement technique, not only health-friendly but also real-time, has become an urgently task. Recent years, AE measurement technique, considered as a nonintrusive method, has attracted considerable attentions and has been applied to measure average particle size.[18,19,21] However, its application to on-line measurement of PSD is rarely reported.

The earlier analyses of structure characteristics of AE signals indicated that (1) microscale signals consisting of 1–5 level detailed signals totally reflect the information about particles motion, and (2) mesoscale signals consisting of 6–7 level detailed signals partially reflect the information about particles motion. In contrast, there are only two levels detailed microscale signals of pressure signals that totally represent the information about particles motion, while other seven levels detailed mesoscale signals just partially or even not at all represent the information about particles motion coupled with bubbles motion. It could thus be implied that AE technique is more suitable than pressure technique for measurements of average particle size and PSD. Therefore, as an illustrative application example of AE technique, a prediction model was established to measure PSD, as well as average particle size.

For n identical particles (with a diameter of d_p and a mass of m) impact on an area ΔA of the wall of a bed with the normal velocity of v, the resultant average force $\langle F(t)\rangle$ in a time interval T is given by[16]

$$\langle F(t)\rangle = \frac{\int_0^T F(t)dt}{T} = \frac{2mv\int_0^T \sum_{i=1}^{n}\delta(t-t_i)dt}{T} \tag{22}$$

where $\delta(t)$ is Dirac delta function, and t_i is the arrival time of the ith particle on the wall. Let f_p denote the average arrival frequency of the particles on the wall, the number of collisions between particles and wall in a time interval T is $f_\mathrm{p}\cdot T$. Thus, the average force $\langle F(t)\rangle$ in an unit time interval can be expressed as,

$$\langle F(t)\rangle = \frac{2mv\int_0^T \sum_{i=1}^{n}\delta(t-t_i)dt}{T} = \frac{2mvf_\mathrm{p}T}{T} = 2mvf_\mathrm{p} \tag{23}$$

Consequently, the acoustic pressure generated on an area ΔA of the wall can be given by

$$P_\mathrm{AE} = \frac{\eta\langle F(t)\rangle}{\Delta A} = \frac{2\eta mvf_\mathrm{p}}{\Delta A} \tag{24}$$

where η is the transformation efficiency from the collision pressure to acoustic pressure detected by AE sensor. There are several factors that can take significant effects on the transformation efficiency η, such as the distance between collision position and sampling position, and the operation conditions of experimental apparatus. Let ρ_b and w denote the particle density near the wall and the mass fraction of particles with a size of d_p respectively, then the number concentration C (number$\cdot$m^{-3}) of particles with a size of d_p can be expressed as $C = \rho_\mathrm{b}\cdot w/m$. Consequently, the average arrival frequency of the particles on the wall, f_p, can be given by

$$f_\mathrm{p} = C\cdot\frac{\Delta Av}{\Delta A} = \frac{\rho_\mathrm{b}wv}{m} \tag{25}$$

Therefore, for particles (with d_p in diameter, m in mass, and w in mass fraction) impact on an area ΔA of the wall, the energy of signals received by AE sensor, E, during a time interval T, can be calculated by

$$E(d_\mathrm{p}) = \int_D^T P_\mathrm{AE}\Delta Av dt = \int_D^T 2\eta\rho_\mathrm{b}v^3 w dt \tag{26}$$

It can be seen from Eq. 26 that the signal energy E is a function of transformation efficiency η, particle density near the wall ρ_b, particle normal velocity v and particle mass fraction m. By maintaining the operation conditions constant, such as superficial gas velocity and level of material, both the transformation efficiency η and the particle density near the wall ρ_b could be considered roughly to be constant. Meanwhile, under constant operation conditions, the normal velocity v is mainly related to the particle size distribution. It is, therefore, implied that the signal energy can be consider to be a function of PSD under specific operation conditions.

For particles with K different sizes jointly impact on the wall, the total mixed signal energy, E^mix, can be calculated based on the linear superposition principle of acoustic energy as follows:

$$E^\mathrm{mix} = \sum_{k=1}^{K} E^k\cdot w_k \tag{27}$$

where E^k and w_k are the signal energy and mass fraction of kth type of particles with a size of $d_{\mathrm{p},k}$ respectively. In view of the independent feature of acoustic propagation, different acoustic waves generated from particles with different sizes impact on the wall will maintain their own characteristics (e.g., frequency, and amplitude etc.). Hence, it can be further supposed that the energy of acoustic on different levels can be maintained constant under acoustic superposition. According to wavelet analysis, the conservation relationships of signals for mixed particle sizes and signals for single particle size at different detailed levels, as well as approximated level, can be given as follows:

$$E_{j,D}^\mathrm{mix} = \sum_{k=1}^{K} E_{j,D}^k w_k, \quad j = 1,\ldots,L \tag{28}$$

Table 3. Comparisons of Average Particle Size and Particle Size Distribution Measured Using AE Method and Sieve Method in Laboratory Scale and Plant Scale Apparatuses

Type	Method		Mass Fractions for Different Particle Sizes (%, mm)							Average Particle Size (mm)
			2	1.19	0.71	0.5	0.36	0.18	0.14	
LLDPE	Sieve method		0.50	6.60	4.00	27.70	42.60	9.90	9.30	0.4396
	AE method	Laboratory scale	1.00	6.33	3.90	26.20	43.37	9.30	9.90	0.4407
		Plant scale	0.39	8.40	4.40	25.70	40.10	11.00	10.10	0.4440
HDPE	Sieve method		15.80	31.80	15.90	29.80	4.10	2.60	0.00	0.9758
	AE method	Laboratory scale	14.80	33.60	15.00	27.60	2.60	4.40	2.00	0.9604
		Plant scale	14.10	36.00	12.60	30.00	2.90	2.30	2.10	0.9674
BPE	Sieve method		4.53	9.50	19.74	20.47	32.89	12.87	0.00	0.5877
	AE method	Laboratory scale	4.80	11.60	16.80	19.90	30.90	13.00	3.00	0.5917
		Plant scale	5.10	13.80	17.90	16.60	31.10	13.30	2.20	0.6153

$$E_{\mathrm{L,A}}^{\mathrm{mix}} = \sum_{k=1}^{K} E_{\mathrm{L,A}}^{k} \cdot w_k \tag{29}$$

where L is the number of decomposed levels; $E_{j,D}^{k}$ and $E_{L,D}^{k}$ are the energies of detailed signal on the level of j and approximated signal on the level of L for the kth type of particles with a size of $d_{\mathrm{p},k}$ respectively; and $E_{j,\mathrm{D}}^{\mathrm{mix}}$ and $E_{\mathrm{L,D}}^{\mathrm{mix}}$ are the energies of detailed signal on the level of j and approximated signal on the level of L for mixed particle sizes respectively. Let λ_k denote a ratio of signal energy for kth type of particles and signal energy for mixed particle sizes, which is defined as

$$\lambda_k = \frac{E^k}{E^{\mathrm{mix}}}, \quad k = 1, \ldots, K \tag{30}$$

Therefore, Eqs. 28 and 29 can be further transformed as follows:

$$\mathrm{EP}_{j,\mathrm{D}}^{\mathrm{mix}} = \sum_{k=1}^{K} \lambda_k \mathrm{EP}_{j,\mathrm{D}}^{k} \cdot w_k, \quad j = 1, \ldots, L \tag{31}$$

$$\mathrm{EP}_{\mathrm{L,A}}^{\mathrm{mix}} = \sum_{k=1}^{K} \lambda_k \cdot \mathrm{EP}_{\mathrm{L,A}}^{k} \cdot w_k \tag{32}$$

where $\mathrm{EP}_{j,\mathrm{D}}^{k}$ and $\mathrm{EP}_{\mathrm{L,D}}^{k}$ are the energy percentages of detailed signal on the level of j and approximated signal on the level of L for the kth type of particles calculated based on Eqs. 12 and 13 respectively; and $\mathrm{EP}_{j,\mathrm{D}}^{\mathrm{mix}}$ and $\mathrm{EP}_{\mathrm{L,D}}^{\mathrm{mix}}$ are the energy percentages of detailed signal on the level of j and approximated signal on the level of L for mixed particle sizes calculated based on Eqs. 12 and 13, respectively. Hence, after calibrations of the values of λ_k ($k = 1, \ldots, K$), as well as the values of $\mathrm{EP}_{j,\mathrm{D}}^{k}$ and $\mathrm{EP}_{\mathrm{L,D}}^{k}$, where $k = 1, \ldots, K$ and $j = 1, \ldots, L$, the mass fractions of different types of particles, w_k ($k = 1, \ldots, K$), can be obtained by solving the linear equations shown in Eqs. 31 and 32. Because the earlier study on structure characteristics of AE signals has implied that the macrosignals consisting of the detailed signals on the levels of 8 and 9 and the approximated signals on the level of 9 do not reflect the information about particles motion at all, it is supposed that decomposing the AE signals into larger than 7 levels will not provide extra information for prediction of PSD, which has been demonstrated based on our experimental results. The number of decomposed levels, L, is thus set equal to 7 in the present study.

To illustrate the effectiveness of the PSD prediction model, the on-line measurement experiments were carried out both in laboratory scale and plant scale gas–solid fluidized beds. Three types of PE particles collected from plant scale plant scale fluidized beds, i.e., LLDPE, HDPE, and BPE, were used as the fluidized particle in laboratory scale fluidized beds. The model parameters in Eqs. 31 and 32 were calibrated based on the AE signals collected from laboratory scale apparatus. The results are shown in Table 3. It can be seen from Table 3 that the mass fractions of different particle sizes measured using AE method is consistent with that measured using sieve method. Define the average absolute deviation, AAD, of PSD prediction between AE method and sieve method as

$$\mathrm{AAD} = \frac{1}{K} \sum_{k=1}^{K} \left| w_k^{\mathrm{sieve}} - w_k^{\mathrm{AE}} \right| \tag{33}$$

where w_k^{sieve} and w_k^{AE} are the mass fractions of the kth type of particles measured by sieve method and AE method respectively; and $K = 7$ is the number of types of particles. It can be calculated from Table 3 that (1) in the laboratory scale experiments, the values of AAD are 0.62%, 1.60%, and 1.57% for LLDPE, HDPE, and BPE respectively, and (2) in the plant scale experiments, the values of AAD are 1.26%, 1.86%, and 2.14% for LLDPE, HDPE, and BPE respectively.

Moreover, because the average particle size can be calculated based on the measured PSD, the average particle size measured by AE method and sieve method are also compared and shown in Table 3. It can be calculated from Table 3 that (1) in the laboratory scale experiments, the relative deviation of average particle size between AE method and sieve method are 0.25%, 1.57%, and 0.67% for LLDPE, HDPE, and BPE respectively, and (2) in the plant scale experiments, the relative deviation of average particle size between AE method and sieve method are 0.99%, 0.86%, and 4.69% for LLDPE, HDPE, and BPE respectively. The results of plant scale experiments for the prediction of average particle size by the PSD prediction model proposed in this study show superior performance to the frequency model proposed by the Jiang et al.[21] The superiority of PSD prediction model could be supported by the fact that wavelet transform analysis is more suitable to deal with nonstationary signals than Fourier transform analysis. In a word, the results

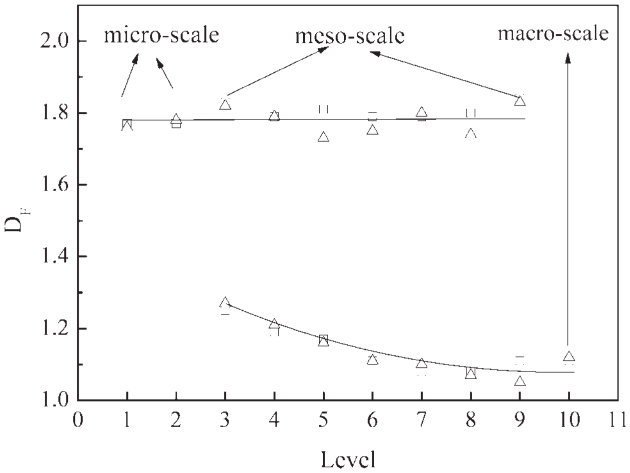

Figure 7. Structure diagram of AE signals in liquid–solid stirred tank.

Glass bead size: 0.5 mm (□); 0.7 mm (△).

illustrate that the AE measurement in combination with the PSD model provide an effective tool to on-line measurement of both average particle size and PSD.

Structure characteristics comparison of AE signals in gas–solid and liquid–solid systems

In view of the fact that the physical characteristics of different multiphase systems are in general different, the structure characteristics of AE signals collected from different multiphase systems could exist great differences. The structure characteristics of AE signals collected from gas–solid fluidized bed and liquid–solid stirred tank were compared in this section. Two experiments in liquid–solid stirred tank under complete suspension condition were conducted with the solids concentration of 0.13 g mL^{-1} and impeller speed of 8.33 r s^{-1} for two different glass bead diameters of 0.5 mm and 0.7 mm. The original AE signals from two different measurements with respect to two different glass bead sizes were decomposed into 1–9 level detailed signals and level-9 approximated signal using Daubechies 2nd order wavelet transform. Figure 7 shows the structure diagram of AE signals by resorting to R/S analysis of the decomposed signals. An example of three-scale resolution of AE signals for glass bead with a diameter of 0.5 mm is shown in Figure 8.

Compared the structure diagram of AE signals in gas–solid fluidized bed shown in Figure 5 with the structure diagram of AE signals in liquid–solid stirred tank shown in Figure 7, it is found that (1) the microscale signals consisting of 1–2 level detailed signals in liquid–solid stirred tank is much narrower than the microscale signals consisting of 1–5 level detailed signals in gas–solid fluidized bed, and (2) the mesoscale signals consisting of 3–9 level detailed signals in liquid–solid stirred tank is much wider than the mesoscale signals consisting of 6–7 level detailed signals in gas–solid fluidized bed. Moreover, the energy percentages of AE signals in liquid–solid stirred tank are 45.5%, 53.2%, and 1.3% for microscale, mesoscale, and macroscale signals respectively. This means that the energy of AE signals in liquid–solid stirred tank is approximately distributed equally by microscale and mesoscale signals, which is different from the AE signals in gas–solid fluidized bed whose most energy is distributed mainly by microscale signals. These observed structure characteristics differences between liquid–solid and gas–solid systems could be supported by the fact that (1) in gas–solid fluidized bed, acoustic emissions are generated

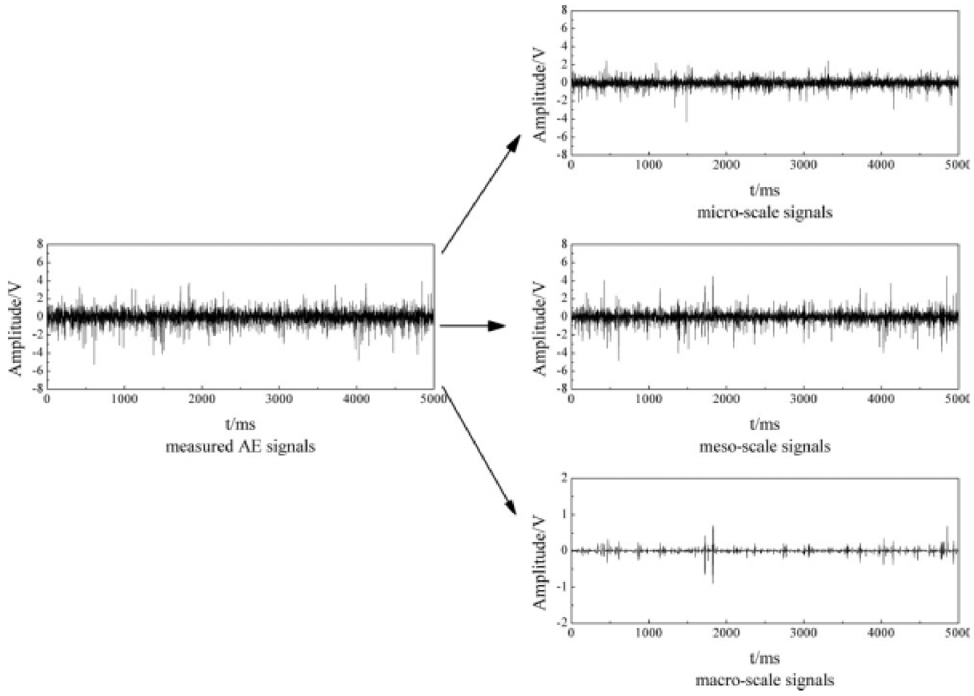

Figure 8. Resolution of measured AE signals into three scales for glass bead with a diameter of 0.5 mm.

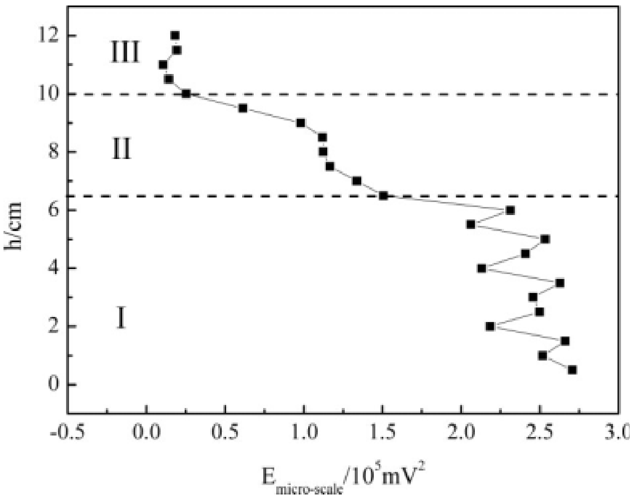

Figure 9. Energy profile of AE signals in microscale.

mainly by the collisions between particles and wall, and (2) in liquid–solid stirred tank, acoustic emissions are generated not only by the collisions between particles and tank, but also by the collisions between liquids and tank. On the other hand, under the complete suspension condition, the most particles are dispersed in suspension phase, and the frequency band of collisions between liquids and tank could be comparable to that of collisions between those particles and tank, which may cause the wide mesoscale signals in liquid–solid tank.

In a word, structure characteristics of AE signals measured in different multiphase systems could be distinguished based on structure diagram and energy distribution analysis. Investigating the underlying structure characteristics of signals could provide primary information not only to judge whether this measurement technique is suitable for a particular application, but also to reveal possible difficulties encountered. Moreover, it could be helpful to extract the most physical meaningful characteristic features for a particular application based on structure characteristics of signals.

Measurement of suspension height and liquid level

The critical impeller speed[32] and suspension height[33] are two of the most important properties to measure the effectiveness of solid suspension in a stirred tank. The critical impeller speed and suspension height provide measures of the off-bottom suspension conditions and the solids distribution conditions of solid particles respectively. For obtaining a more complete picture of the effectiveness of solid suspension, it has been suggested that both critical impeller speed and suspension height should be considered together.[33,34] Hence, developments of quick and accurate monitoring techniques for measuring both two properties can play important roles in the design and operation of stirred tank. Previous study of our research group[22] has illustrated that AE technique can be considered as an appropriate method for measuring the critical impeller speed based on multiscale analysis of AE signals. In this section, we will further extend AE technique to measurement of the suspension height in terms of aforementioned structure characteristics study of AE signals.

According to solids concentration profiles, van der Westhuizen et al.[34] defined the suspension height as the height where the profile dropped below half the bulk solids concentration. Below the suspension height, a comparatively homogeneous solids concentration could be observed under complete suspension condition; whereas above the suspension height, solids concentration dropped sharply.[34] By analysis of the structure characteristics of AE signals, it can be found that AE signals in microscale represent totally the dynamics of solid phase. Moreover, it has been found that solids concentration displays an approximate linear relationship with the energy of AE signals in microscale by maintaining the other operation conditions constant. Therefore, the energy of AE signals in microscale, to a certain extent, can be considered as an indicator of solids concentration, and it is selected as a feature for measuring the suspension height. Furthermore, by investigating the energy profile of AE signals in microscale, a criterion is established to measure the suspension height described as follows.

One experiment in liquid–solid stirred tank under complete suspension condition was conducted to develop the criterion for determination of the suspension height, with the solids concentration of 0.016 g mL^{-1} and impeller speed of 9.17 r s^{-1} for glass bead diameters of 0.7 mm. Twenty-four sets of AE signals were measured corresponding to 24 different axial heights. Figure 9 shows the energy profile of AE signals in microscale, which plot the energy of AE signals in microscale, on the horizontal axis vs. the axial height in the stirred tank, on the vertical axis. It is noticeable that the energy of AE signals in microscale exhibit two times of step changes with respect to the axial height. Thus, the energy distribution of AE signals microscale in the tank can be divided into three regions as shown in Figure 9. It is found that (1) in the region I ($0 \leq h \leq 6.5$ cm), the energy of AE signals in microscale is relative higher and fluctuate around 25,000 mV^2, (2) in the region II ($6.5 \leq h \leq 9.5$ cm), the energy of AE signals in microscale decreases sharply, and the mean energy is approximately equal to half the energy in region I, and (3) in the region III ($9.5 \leq h \leq 12$ cm), the

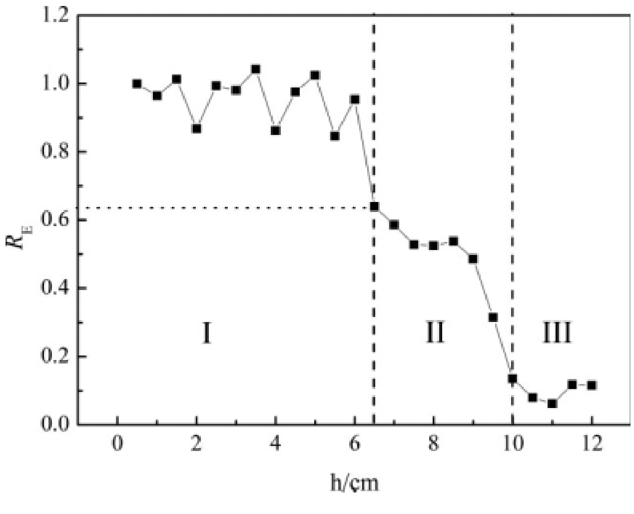

Figure 10. Height vs. R_E.

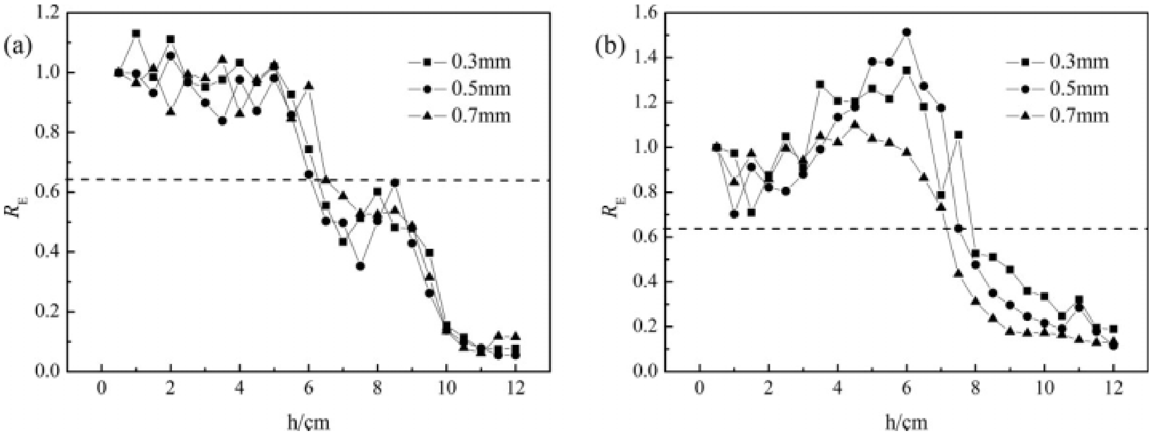

Figure 11. R_E profiles for two types of impellers: (a) 6-bladed disk turbine; (b) 2-bladed paddle impeller.

energy of AE signals in microscale drops to 2500 mV^2 and tends to be stable. Based on these observations and the relationship discussed earlier between the energy of AE signals in microscale and solids concentration, it can be further indicated that (1) region I has the highest solids concentration and its distribution of solids concentration is relatively uniform, (2) solid concentration in region II is about 50% of that in region I and it displays an roughly decrease trend with respect to the height, and (3) solid concentration in region III is about 10% of that in region I and it tends to be stable. Thus, by combing the aforementioned discussions with the definition of the suspension height,[34] the height corresponding to the boundary between regions I and II can be considered as the suspension height.

However, in view of the fact that the energy values of AE signals in microscale may exist great differences in different impeller speeds and solids concentrations, a more general dimensionless feature, R_E, is proposed to measure the suspension height defined as follows:

$$R_E = \frac{E_n}{\frac{1}{n}\sum_{i=1}^{n} E_i} \tag{34}$$

where n ($n = 1,\ldots,24$) denotes the nth sampling point of AE signals, and E_n denotes the energy values of AE signals in microscale for the nth sampling point. Figure 10 shows the plot of the height against the value of R_E, also called R_E profile in the present study. It is noticeable that the R_E profile shown in Figure 10 exhibits a similar behavior of energy profile of AE signals in microscale shown in Figure 9. Thus, a criterion with the value of R_E being equal to 0.64 is proposed to measure the suspension height.

To validate the effectiveness of the established criterion for measuring the suspension height, several on-line measurement experiments in liquid–solid stirred tank under complete suspension condition were carried out with two types of impellers (i.e., 6-bladed disk turbine and 2-bladed paddle impeller) for three different glass bead diameters (i.e., 0.3, 0.5, and 0.7 mm). All experiments were conducted with the solids concentration of 0.016 g mL^{-1} and impeller speed of 9.17 r s^{-1}. Figures 11a, b show two R_E profiles for 6-bladed disk turbine and 2-bladed paddle impeller, respectively. It is indicated that all R_E profiles shown in Figures 11a, b exhibit similar behaviors of R_E profile shown in Figure 10. Further, according to the aforementioned criterion, the suspension heights for different types of impellers and glass bead diameters can be determined from Figures 11a, b and the results are shown in Table 4.

As Reiger et al. stated,[35] visual method is one of the best measurement techniques for measuring the suspension height. So the visual method is adopted in the present study to performance validation of our proposed AE method. However, it should be noted that the visual method can not be used in opaque stirred tank. It can be seen from Table 4 that the average absolute relative deviations, AARD, between AE method and sieve method are 5.54% and 7.76% for experiments with 6-bladed disk turbine and 2-bladed paddle impeller, respectively. The results demonstrate that the proposed criterion for measuring the suspension height has fairly good applicability under experiments with different types of impellers and glass bead diameters. Thus, AE technique combined with the proposed criterion provide an effective method to on-line measurement of the suspension height. On the other hand, AE technique is also validated to be an appropriate method for measuring the critical impeller speed according to the previous study of our research group.[22]

Table 4. Comparison of the Suspension Heights Measured Using AE and Visual Method

	h (cm, 6 Bladed Disk Turbine)			*h* (cm, 2 Bladed Paddle Impeller)		
Particle size (mm)	AE method	Visual method	AARD (%)	AE method	Visual method	AARD (%)
0.3	6.4	6.8	5.54	7.9	8.5	7.76
0.5	6.1	6.6		7.5	8.2	
0.7	6.5	6.3		7.2	7.8	

Hence, AE technique combined with appropriate model can be applied to on-line measurements of not only the critical impeller speed but also the suspension height for industrial process, and is convenience to help the design and operation of stirred tank.

Conclusions

This study investigated thoroughly the structure characteristics of AE signals measured in gas–solid fluidized bed and liquid–solid stirred tank by resorting to wavelet transform and R/S analysis. A general criterion was established to resolve AE signals to three characteristic scales based on the Hurst exponent characteristics: microscale signals with all Hurst exponents less than 0.5; mesoscale signals with some Hurst exponents less than 0.5 and some Hurst exponents greater than 0.5; macroscale signals with all Hurst exponents greater than 0.5. Meanwhile, structure diagram, a plot of fractal dimension against level, was introduced. The main findings of the present study can be summarized as follows:

1. By the comparison of structure characteristics between AE and pressure signals in gas–solid fluidized bed, it was found that (1) AE signals in microscale consisting of 1–5 level detailed signals is much wider than pressure signals in microscale consisting of 1–2 level detailed signals, and (2) AE signals in mesoscale consisting of 6–7 level detailed signals is much narrower than pressure signals in mesoscale consisting of 3–9 level detailed signals. Further, energy distribution analysis revealed that the most energy both in AE signals and pressure signals were distributed mainly by the microscale and mesoscale signals respectively. These observations imply that AE signals represent mainly microscale particles motion while pressure signals represent mainly mesoscale interaction dynamics between particles motion and bubbles motion. Therefore, AE technique could be considered as an effective tool to measure particle-related properties in gas–solid fluidized bed.

2. Based on the thorough investigation of structure characteristics of AE signals measured in gas–solid fluidized bed, it has been supposed that AE technique could be an appropriate method for measuring particle-related properties in gas–solid fluidized bed. Therefore, a prediction model was proposed to measure particle size distribution (PSD) and average particle size for three types of PE, i.e., LLDPE, HDPE, and BPE. The on-line measurements of PSD and average particle size were performed both in laboratory scale and plant scale fluidized beds. The results showed that (1) average absolute deviation between AE method and manual sieve method were no more than 2.14% for PSD prediction, and (2) relative deviation between AE method and sieve method were no more than 4.69% for average particle size prediction. The results, therefore, invalidated that AE technique combined with a prediction model could provide an effective method to on-line measurements of PSD and average particle size in gas–solid fluidized bed.

3. The structure characteristics of AE signals collected from gas–solid fluidized bed and liquid–solid stirred tank were also compared based on structure diagram and energy distribution analysis. The results indicated that there exist great differences in the structure characteristics of AE signals measured in gas–solid fluidized bed and liquid–solid stirred tank. Compared with the structure diagram of AE signals in fluidized bed, it was found microscale and mesoscale of AE signals in liquid–solid stirred tank becomes narrow and broadens respectively. On the other hand, the energy of AE signals in liquid–solid stirred tank was approximately distributed equally by microscale and mesoscale signals, which was different from the AE signals in gas–solid fluidized bed whose most energy is distributed mainly by microscale signals.

4. Based on the thorough investigation of structure characteristics of AE signals measured in stirred tank, it was found that AE signals in microscale represent totally the dynamics of particles motion. Therefore, a criterion based on the energy profile of AE signals in microscale and R_{E} profile was established to measure the suspension height. The results showed that the average absolute relative deviations between AE method and sieve method are 5.54% and 7.76% for experiments with 6-bladed disk turbine and 2-bladed paddle impeller respectively. The results, therefore, invalidated that AE technique combined with a proposed criterion could provide an effective method to on-line measurement of the suspension height in a stirred tank.

Hence, the aforementioned findings indicate that investigations of the structure characteristics of AE signals are helpful not only to understand a relatively complete picture of hydrodynamics of multiphase systems, but also to extract the most useful information from the original signals with respect to a particular measurement requirement. However, the present study is preliminary and needs to be further investigated. On the other hand, analyses of structure characteristics based on structure diagram and energy distribution need to be further extended to other multiphase systems (e.g., gas–liquid, gas–solid–liquid, and gas– liquid–liquid etc.). On the one hand, it needs to further develop more effective on-line models for process monitoring with respect to AE technique based on the studies of structure characteristics, as well as advanced statistical and intelligent methods.

Acknowledgments

The authors acknowledge the following scientists and students in Zhejiang University: Hou Linxi, Huang Zhengliang, Jiang Xiaojing, and Zhang Xiaohuan. The field data presented here would have not been accomplished without their assistance. The authors are also thankful for the support of the National Natural Science Foundations of China (20676114, 20490205 and 20736011) and National High Technology Research and Development Program of China (2007AA04Z182).

Notation

AAD = average absolute deviation
AARD = average absolute relative deviations
$A_j(t)$ = approximated signal at each scale j, mV
$c_{j,k}$ = approximated coefficients, dimensionless
C = number concentration of particles, number·m^{-3}
$d_{j,k}$ = detailed coefficients, dimensionless
d_{p} = particle diameter, mm
D_{F} = fractal dimension, dimensionless
$D_j(t)$ = detailed signal at each scale j, mV
E = total energy of $x(t)$, mV^2
$E_{j,\mathrm{D}}$ = energy of the detailed signal $D_j(t)$, mV^2
$E_{\mathrm{L,A}}$ = energy of the approximated signal $A_{\mathrm{L}}(t)$, mV^2
$\mathrm{EP}_{j,\mathrm{D}}$ = energy percentage of the detailed signal $\mathrm{D}_j(t)$, dimensionless
$\mathrm{EP}_{\mathrm{L,A}}$ = energy percentage of the approximated signal $A_{\mathrm{L}}(t)$, dimensionless

f_{p} = average arrival frequency of the particles on the wall, number·s^{-1}
$\langle F(t) \rangle$ = average force in a time interval T, kg m s^{-2}
$g(n)$ = high-pass filter coefficients, dimensionless
$h(n)$ = low-pass filter coefficients, dimensionless
H = Hurst exponent, dimensionless
L = number of decomposition levels, dimensionless
m = particle mass, kg
M_k = mean, V
N = length of signal, dimensionless
P_{AE} = acoustic pressure generated on an area ΔA, kg $(\mathrm{m\ s})^{-1}$
R_k = range, dimensionless
R_{E} = dimensionless feature in Eq. 34
S_k = standard deviation
T = time interval, s
v = normal velocity, m s^{-1}
V_j = approximated versions of the signal on level j
w = mass fraction of particles, dimensionless
W_j = detailed versions of the given signal on level j
$x(t)$ = discrete signal, mV

Greek letters

$\delta(t)$ = Dirac delta function
η = transformation efficiency, dimensionless
λ_k = signal energy ratio of kth type of particle and mixed particle sizes, dimensionless
ρ_{b} = particle density near the wall, kg m^{-3}
τ = time scale, s
$\varphi(t)$ = wavelet function
$\phi(t)$ = scaling function
ΔA = area, m^2

Literature Cited

1. van Wachem BGM, Schouten JC, van den Bleek CM, Krishna R, Sinclair JL. CFD modeling of gas-fluidized beds with a bimodal particle mixture. *AIChE J*. 2001;47:1292–1302.
2. Syamlal M, O'Brien TJ. Fluid dynamic simulation of O-3 decomposition in a bubbling fluidized bed. *AIChE J*. 2003;49:2793–2801.
3. Buwa VV, Ranade VV. Characterization of dynamics of gas-liquid flows in rectangular bubble columns. *AIChE J*. 2004;50:2394–2407.
4. Khopkar AR, Ranade VV. CFD simulation of gas-liquid stirred vessel: VC, S33, and L33 flow regimes. *AIChE J*. 2006;52:1654–1672.
5. Owoyemi O, Mazzei L, Lettieri P. CFD modeling of binary-fluidized suspensions and investigation of role of particle-particle drag on mixing and segregation. *AIChE J*. 2007;53:1924–1940.
6. van Wachem B, Sasic S. Derivation, simulation and validation of a cohesive particle flow CFD model. *AIChE J*. 2008;54:9–19.
7. Wang HG, Yang WG, Senior P, Raghavan RS, Duncan SR. Investigation of batch fluidized-bed drying by mathematical modeling, CFD simulation and ECT measurement. *AIChE J*. 2008;54:427–444.
8. Werther J. Measurement techniques in fluidized beds. *Powder Technol*. 1999;102:15–36.
9. Boyer C, Duquenne AM, Wild G. Measuring techniques in gas-liquid and gas-liquid-solid reactors. *Chem Eng Sci*. 2002;57:3185–3215.
10. Li JH, Kwauk M. Exploring complex systems in chemical engineering-the multi-scale methodology. *Chem Eng Sci*. 2003;58:521–535.
11. Ge W, Chen FG, Gao J, Gao SQ, Huang J, Liu XX, Ren Y, Sun QC, Wang LM, Wang W, Yang N, Zhang JY, Zhou GZ, Li JH. Analytical multi-scale method for multi-phase complex systems in process engineering-bridging reductionism and holism. *Chem Eng Sci*. 2007;62:3346–3377.
12. Lu XS, Li JH. Wavelet analysis of pressure fluctuation signals in a bubbling fluidized bed. *Chem Eng J*. 1999;75:113–119.
13. Zhao GB, Yang YR. Multiscale resolution of fluidized-bed pressure fluctuations. *AIChE J*. 2003;49:869–882.
14. Briongos JV, Aragón JM, Palancar MC. Phase space structure and multi-resolution analysis of gas-solid fluidized bed hydrodynamics. Part I. The EMD approach. *Chem Eng Sci*. 2006;61:6963–6980.
15. Yang TY, Leu LP. Study of transition velocities from bubbling to turbulent fluidization by statistic and wavelet multi-resolution analysis on absolute pressure fluctuations. *Chem Eng Sci*. 2008;63:1950–1970.
16. Cody GD, Goldfarb DJ, Storch GV Jr, Norris AN. Particle granular temperature in gas fluidized beds. *Powder Technol*. 1996;87:211–232.
17. Cody GD, Bellows RJ, Goldfarb DJ, Wolf HA, Storch GV Jr. A novel non-instrusive probe of particle motion and gas generation in the feed injection zone of the feed riser of a fluidized bed catalytic cracking unit. *Powder Technol*. 2000;110:128–142.
18. Halstensen M, Esbensen K. New developments in acoustic chemometric prediction of particle size distributions "the problem is the solution." *J Chemom*. 2000;14:463–481.
19. Boyd JWR, Varley J. The uses of passive measurement of acoustic emissions from chemical engineering processes. *Chem Eng Sci*. 2001;56:1749–1767.
20. Hiroyuki T, Toyokazu Y, Huang CC, Sekiguchi I. Monitoring particle fluidization in a fluidized bed granulator with an acoustic emission sensor. *Powder Technol*. 2000;113:88–96.
21. Jiang XJ, Wang JD, Jiang BB, Yang YR, Hou LX. Study of the power spectrum of acoustic emission (AE) by accelerometers in fluidized beds. *Ind Eng Chem Res*. 2007;46:6904–6909.
22. Ren CJ, Jiang XJ, Wang JD, Yang YR, Zhang XH. Determination of critical speed for complete solid suspension using acoustic emission method based on multiscale analysis in stirred tank. *Ind Eng Chem Res*. 2008;47:5323–5327.
23. Sasic S, Leckner B, Johnsson F. Time-frequency investigation of different modes of bubble flow in a gas-solid fluidized bed. *Chem Eng J*. 2006;121:27–35.
24. Michel M, Yves M, Georges O, Jean-Michel P. *Wavelets and their Applications*. London: ISTE Publishing Company, 2007.
25. Daubechies I. Orthonormal bases of compactly supported wavelets. *Commun Pure Appl Math*. 1988;41:909–996.
26. Hurst HE. Long-term storage capacity of reservoirs. *Trans Am Soc Civil Eng*. 1951;116:770–808.
27. Fan LT, Neogi D, Yashima M, Nassar R. Stochastic analysis of a three-phase fluidized bed: fractal approach. *AIChE J*. 1990;36:1529–1535.
28. Fan LT, Kang Y, Neogi D, Yashima M. Fractal analysis of fluidized particle behavior in liquid-solid fluidized beds. *AIChE J*. 1993;39:513–517.
29. Briens CL, Briens LA, Hay J, Hudson C, Margaritis A. Hurst's analysis to detect minimum fluidization and gas maldistribution in fluidized beds. *AIChE J*. 1997;43:1904–1908.
30. Mandelbrot BB, Wallis JR. Some long-run properties of geographysical records. *Water Resour Res*. 1969;5:321–340.
31. Mandelbrot BB, Wallis JR. Robustness of the rescaled ranged R/S in the measurement of noncyclic long run statistical dependence. *Water Resour Res*. 1969;5:967–988.
32. Zwietering TN. Suspending of solid particles in liquid by agitators. *Chem Eng Sci*. 1958;8:244–253.
33. Arbiter N, Harris CC, Yap RF. Hydrodynamics of flotation cells. *ASME Trans*. 1969;244:134–148.
34. van der Westhuizen AP, Deglon DA. Evaluation of solids suspension in a pilot-scale mechanical flotation cell: the critical impeller speed. *Miner Eng*. 2007;20:233–240.
35. Reiger F, Ditl P. Suspension of solid particles. *Chem Eng Sci*. 1994;49:2219–2227.

Manuscript received Sep. 8, 2008, and revision received Dec. 21, 2008.